

Image-based axon model highlights heterogeneity in initiation of damage

Lucy M. Wang,^{1,*} Miriam B. Goodman,² and Ellen Kuhl¹

¹Department of Mechanical Engineering, Stanford University, Stanford, California and ²Department of Molecular and Cellular Physiology, Stanford University, Stanford, California

ABSTRACT Head injury simulations predict the occurrence of traumatic brain injury by placing a threshold on the calculated strains for axon tracts within the brain. However, a current roadblock to accurate injury prediction is the selection of an appropriate axon damage threshold. While several computational studies have used models of the axon cytoskeleton to investigate damage initiation, these models all employ an idealized, homogeneous axonal geometry. This homogeneous geometry with regularly spaced microtubules, evenly distributed throughout the model, overestimates axon strength because, in reality, the axon cytoskeleton is heterogeneous. In the heterogeneous cytoskeleton, the weakest cross section determines the initiation of failure, but these weak spots are not present in a homogeneous model. Addressing one source of heterogeneity in the axon cytoskeleton, we present a new semiautomated image analysis pipeline for using serial-section transmission electron micrographs to reconstruct the microtubule geometry of an axon. The image analysis procedure locates microtubules within the images, traces them throughout the image stack, and reconstructs the microtubule structure as a finite element mesh. We demonstrate the image analysis approach using a *C. elegans* touch receptor neuron due to the availability of high-quality serial-section transmission electron micrograph data sets. The results of the analysis highlight the heterogeneity of the microtubule structure in the spatial variation of both microtubule number and length. Simulations comparing this image-based geometry with homogeneous geometries show that structural heterogeneity in the image-based model creates significant spatial variation in deformation. The homogeneous geometries, on the other hand, deform more uniformly. Since no single homogeneous model can replicate the mechanical behavior of the image-based model, our results argue that heterogeneity in axon microtubule geometry should be considered in determining accurate axon failure thresholds.

SIGNIFICANCE As one of the most common pathological features of traumatic brain injury, diffuse axonal injury leads to loss of consciousness and cognitive impairment. Scientists employ computational modeling in concert with experimental approaches to study the initiation of damage within the axon cytoskeleton and to determine critical failure thresholds. However, past computational studies have all assumed an idealized, homogeneous geometry for the microtubules within the cytoskeleton. This approach overestimates axon strength because the axon cytoskeleton is heterogeneous, and the weakest cross section governs the initiation of damage. Our image-based approach to generating microtubule geometry naturally incorporates the structural heterogeneity of the microtubules in the axon cytoskeleton and highlights the need to consider structural heterogeneity in studies of axon damage.

INTRODUCTION

Every year, an estimated 69 million people suffer from traumatic brain injuries worldwide (1). In the United States alone, over one million occur each year, resulting in over 50,000 deaths (2). Individuals who have sustained a traumatic brain injury experience a wide range of cognitive, emotional, and behavioral disabilities including impaired

attention and memory, personality change, and mood disorders (3). Studies have identified that a key cause of functional impairment in traumatic brain injury is axon damage (4). Axons are long extensions of neurons that conduct electrical impulses and distribute information throughout the brain. They are a frequent lesion site in injury, and axon damage has been linked to coma (5), cognitive impairment, and the development of neurodegenerative diseases such as Alzheimer's disease (6).

Since standard medical imaging techniques cannot easily spot axon damage, scientists have turned to computational

Submitted May 23, 2022, and accepted for publication November 28, 2022.

*Correspondence: lwang8@stanford.edu

Editor: Kristen Verhey.

<https://doi.org/10.1016/j.bpj.2022.11.2946>

© 2022 Biophysical Society.



models to aid the study of traumatic brain injury. Finite element simulations link measured impact forces and head accelerations to the deformation of the skull and brain (7–9). To predict brain injury, various injury criteria are applied to simulation results. Several injury criteria including principal strains and stresses have been evaluated, but axon strain has shown the highest correlation with the occurrence of diffuse axonal injury (9).

The use of finite element models of the head to predict injury depends on the specification of an axon damage threshold (10). Several in vitro studies have investigated axon stretch at various magnitudes and rates to find this threshold and to gain insight into damage within the axon (11–13). Neurons in these studies are cultured on compliant substrates that are stretched to damage the axons. These in vitro studies have discovered evidence of damage to both the plasma membrane (13) and the microtubules within the cytoskeleton (12) as a result of stretch. The damaging effects of mechanical stretch on the actin cortex, however, have yet to be studied in vitro despite the mechanoprotective role of the actin cortex in axons (14,15).

The axonal cytoskeleton has a varied and complex structure (16). The major components of the cytoskeleton include loosely bundled microtubules (17), a network of neurofilaments (18), and the cortical actin-spectrin sleeve located just below the plasma membrane (19,20). The structure of the cytoskeleton varies both among different neuron types and among different species (16). Studies have reported microtubule lengths of 9–23 and 6 μm in *C. elegans* mechanosensory and motoneurons, respectively (21,22). Meanwhile, microtubule lengths in the hundreds of microns have been estimated from transmission electron micrograph (TEM) analyses of vertebrate neurons (16,23,24). Similarly, reported values for the number of microtubules per axon cross section range from 22–49 for *C. elegans* mechanosensory neurons to the hundreds for vertebrates and hundreds of thousands for arthropods (16,21,25,26). Furthermore, the presence or absence of neurofilaments interspersed between microtubules leads to differences in microtubule spacing between vertebrates and other organisms (16).

Each major component of the axonal cytoskeleton plays a role in the mechanical behavior of the axon as a whole (15,27). Microtubules and actin filaments have been shown to contribute to the stiffness of the axon in both atomic force microscopy indentation tests (27) and under tensile stretch (15). Furthermore, spectrin has been shown to play a mechanoprotective role in *C. elegans* neurons (14). Cytoskeletal mechanisms in both the microtubule bundle and actin cortex have also been proposed to contribute to the rate-dependent, viscoelastic behavior of the axon (15,28).

In concert with experimental studies, computational modeling is an important tool for evaluating potential modes of failure in the axonal cytoskeleton under mechanical loading (28–31). Modeling axon damage presents a formidable challenge due to the complex, dynamic structure of

the cytoskeleton (16), as well as the lack of specific knowledge of parameters such as the mechanical strength of cross-links between cytoskeletal components (32). To build tractable models, therefore, it is necessary to make strategic assumptions and simplifications while also considering their implications on simulation results.

One such simplification made in past computational studies is the homogeneity of the cytoskeleton. Previous computational models have all used a homogeneous structure for the microtubules and actin cortex within the model (28,29,31). Microtubules in these homogeneous models are densely packed and regularly spaced in a hexagonal lattice, and their number per cross section remains constant throughout the entire model. Furthermore, some models assume that microtubules within the axon model are identical in length (28,31). The microtubule lengths assumed in these computational studies range from 4 (31) to 10 μm (28). The actin cortex, when included, is represented as a homogeneous cylinder (31). In determining axon failure thresholds, using a homogeneous geometry will overestimate axon strength because failure is determined by the weakest cross section in the cytoskeleton. A homogeneous geometry ignores the potential existence of a weak spot that might be more susceptible to injury.

In reality, the axonal cytoskeleton is heterogeneous. Studies of the microtubule architecture in axons have shown that the number of microtubules per cross section can vary significantly along the axon and that microtubules exhibit a range of different lengths (16,21–23). A study of axon stretch has also found that strain is heterogeneous within the axon (33). Based on imaging docked mitochondria as fiducial markers, global axonal stretch evokes spatial variation in local strains (33).

While other cytoskeletal components such as the actin cortex contribute significantly to the mechanical behavior of the axon (15), we choose here to focus solely on the microtubule bundle. Deformation of the microtubule bundle will likely not exactly mirror that of the whole axon as this would require rigid attachment to the plasma membrane and possibly dynamic rearrangement of microtubule cross-links to accommodate large deformations (28). However, this simplified structure facilitates our investigation of the importance of heterogeneity because of the availability of serial-section TEMs (ssTEMs) to inform the microtubule geometry of our axon model (34).

To investigate the significance of heterogeneity in the microtubule architecture on axonal mechanics, we present a new image analysis pipeline using ssTEM data to determine the microtubule geometry of an axon, and we compare its mechanical response with that of a homogeneous microtubule geometry. We use the touch receptor neurons (TRNs) of *C. elegans* as a model system. While *C. elegans* TRNs exhibit structural differences from vertebrate neurons in microtubule number, length, and spacing (16), we chose these neurons as a model system because of their exceptionally

TABLE 1 Model parameters used in tensile simulations

	Value	Unit	Reference
Axon length	15	μm	—
Microtubule stiffness	1.2	GPa	Gittes et al. (36)
Microtubule area	400	nm^2	Suresh et al. (37)
Cross-link stiffness	10	MPa	Mallik et al. (38)
Cross-link area	1	nm^2	De Rooij et al. (39)
Cytosol dashpot coefficient	$1e - 8$	$\text{N} \cdot \text{s/m}$	—

well-characterized bundle of microtubules, the availability of high-quality ssTEM data sets (34), and experimental studies linking this microtubule bundle to neuronal mechanoprotection (14). Our image-based model inherently incorporates the structural heterogeneity of the axon microtubules and facilitates the study of regional variations in deformation under stretch. Our results emphasize heterogeneity as a new parameter that needs to be considered in future simulations of axon damage.

MATERIALS AND METHODS

Axon finite element model

Each of our axon models consists of a 15- μm -long bundle of microtubules crosslinked by tau-like proteins. For the image-based model, the microtubule geometry comes from the analysis of ssTEM images (34,35). For the homogeneous models, the microtubules are regularly spaced within the cross section (28,29,31). Randomly generated cross-links bind microtubules together in both the image-based and homogeneous models. The following sections provide more detail on these processes for generating model geometry.

In all of the models, we discretize microtubules using linear Bernoulli beam elements and cross-links using linear truss elements. We model both the microtubules and cross-links as linear elastic with Young's moduli of 1.2 GPa and 10 MPa, respectively. Table 1 summarizes the model parameters. In all simulations of tensile loading, we fix the nodes at the proximal end of the model and apply a 250-nm displacement to the nodes at the distal end using displacement control. Rotational degrees of freedom are held fixed for all nodes, and we represent the influence of the cytoplasm viscosity by attaching dashpot elements in the lateral directions at all nodes. All simulations are performed in Abaqus/Standard.

Image analysis for generation of image-based geometry

We analyzed a set of 300 ssTEM images collected from a wild-type *C. elegans* posterior lateral microtubule (PLM) neuron (34,35). Because the contrast in these images was optimized for the visualization of gold-labeled antibodies, the resulting images have lower contrast than typical samples optimized to visualize microtubules. Each image within the data set corresponds to a cross section of 50-nm thickness, covering 15 μm in length along the axon. To retrieve the microtubule architecture from the images, we developed a semiautomated image analysis procedure outlined in Fig. 1. We first apply a template matching algorithm (40) to locate microtubules in each of the 300 ssTEM images. This algorithm compares a template with the ssTEM image and locates regions in the ssTEM image that resemble the template. The algorithm accomplishes this by calculating a normed correlation coefficient between the pixels of the template image and the pixels of a region in the analyzed image. A higher value for the correlation coefficient indicates a higher likelihood of a match between the template and the analyzed image at that location. The algorithm repeats

this analysis until all possible regions in the image have been compared with the template. It then outputs an image whose pixel values equal the correlation coefficients for the corresponding locations in the original ssTEM image. We locate microtubules by thresholding this output image and performing non-max suppression to identify the pixel at the center of each microtubule. For this study, we cropped 24 representative microtubules from the ssTEM image set to use as templates. We merged the results from the comparison with all 24 templates to create the complete list of microtubule locations.

As the ssTEM images include other structures outside of the axon, false positives commonly appear in the template matching. To address this, we take advantage of the observation that the microtubules within the axon are clustered closely together. The false positives, on the other hand, are more sparsely distributed. Occasionally, we detected a single microtubule in another neuron, indicating that this approach can identify microtubules generally and not only the large-diameter microtubules present in the TRNs. We apply density-based spatial clustering of applications with noise (41), a clustering algorithm used in data mining, to identify the largest cluster of match locations in each image. We assume that the match locations excluded from the largest cluster are indeed false positives and discard these points. Fig. 2 shows the results of this analysis on a representative image from the analyzed ssTEM data set. To conclude the identification of microtubules in each individual image, we review the automated results and, if necessary, make final manual adjustments.

After locating the microtubules in each image, we determine how they are connected from image to image. To trace the microtubules throughout the stack of images, we apply an affine registration algorithm (42) to consecutive images to identify which point pairs belong to the same microtubule. After completing this analysis for all images, we transform the final microtubule location and connectivity data into a finite element mesh.

The code developed for the semiautomated image analysis can be found in the following GitHub repository: <https://github.com/LivingMatterLab/ssTEM-Image-Analysis.git>.

Homogeneous microtubule geometry

For comparison with the ssTEM-derived geometry, we created homogeneous geometries based on previous axon damage models (28,29,31). The microtubules in the homogeneous geometries are densely packed in a hexagonal lattice with 45-nm spacing (Fig. 3). The parameter, n_{ring} , specifies the number of rings surrounding the central microtubule and, therefore, the number of microtubules per cross section. Fig. 3 illustrates a homogeneous structure with two rings, $n_{\text{ring}} = 2$. The parameter, L_{MT} , specifies the microtubule length. In building the homogeneous geometry, the initial microtubules at the proximal end of the model are assigned a random length less than or equal to L_{MT} to stagger the discontinuities in each row of microtubules. After the initial microtubules, the rest of the model is built by alternating between 50-nm gaps and microtubules of the full specified length, L_{MT} . The microtubules at the distal end of the model are truncated so that the total model length equals 15 μm to match the ssTEM-based model.

Cross-link density calibration

Since the ssTEM images do not provide a clear view of all the cross-links between the microtubules, we randomly generate cross-links in both the image-based and homogeneous models. The cross-links are evenly spaced, on average, over the length and cross section of the axon, and the number of cross-links is determined by the prescribed cross-link density. To select a value for the cross-link density, we performed simulations of tensile loading on the ssTEM-based model with cross-link densities ranging from 10 to 50 cross-links per μm of microtubule length. We then compared the resulting force-elongation curves with experimental measurements (43).

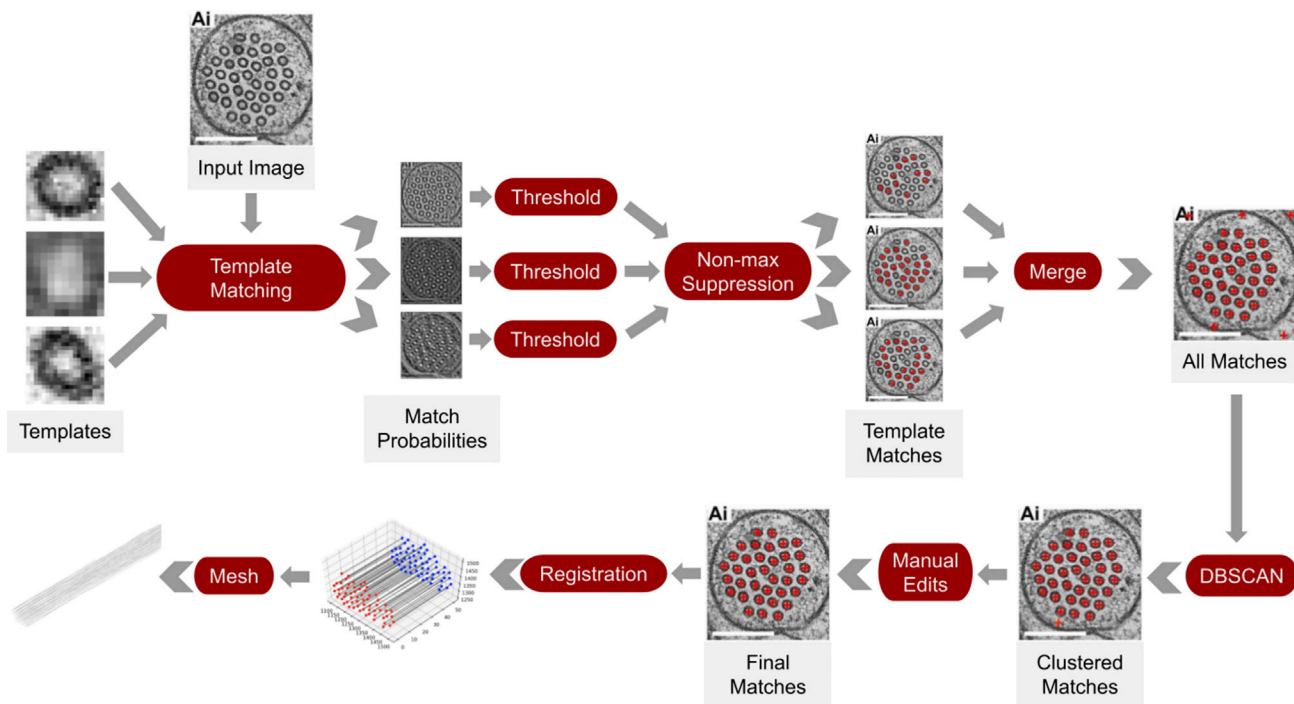


FIGURE 1 Overview of the semiautomated image analysis procedure. Template matching identifies microtubules in the serial-section transmission electron micrographs. Density-based spatial clustering of applications with noise removes false positives, and affine registration traces microtubules throughout the image stack. The final microtubule location and connectivity information is transformed into a finite element mesh. To see this figure in color, go online.

Comparison of image-based and homogeneous geometries

To evaluate the ability of a homogeneous model to replicate the mechanical behavior of the image-based model, we simulated tensile loading on both the image-based model and a collection of 20 homogeneous models with different n_{ring} and L_{MT} values. The values for n_{ring} ranged from 1 to 5, and the corresponding numbers of microtubules per cross section ranged from 7 to 91, spanning the minimum and maximum values seen in the ssTEM analysis. The values for L_{MT} spanned from 2 to 8 μm and were within the range of lengths measured in the image analysis. We did not explore microtubule lengths greater than 8 μm because at these lengths,

the microtubules are more than half the length of the full axon model. As a result, a large proportion of the microtubules are held fixed, and the deformation of the model is greatly affected by the boundary conditions.

Statistical analysis

Spearman's rank correlation was used to analyze the association between microtubule number, the presence of mitochondria, and axon diameter. Spearman's rank correlation was chosen because the analysis does not assume a normal distribution for the data and allows for the analysis of ordinal data. Statistical analysis was performed using the SciPy 1.9.1

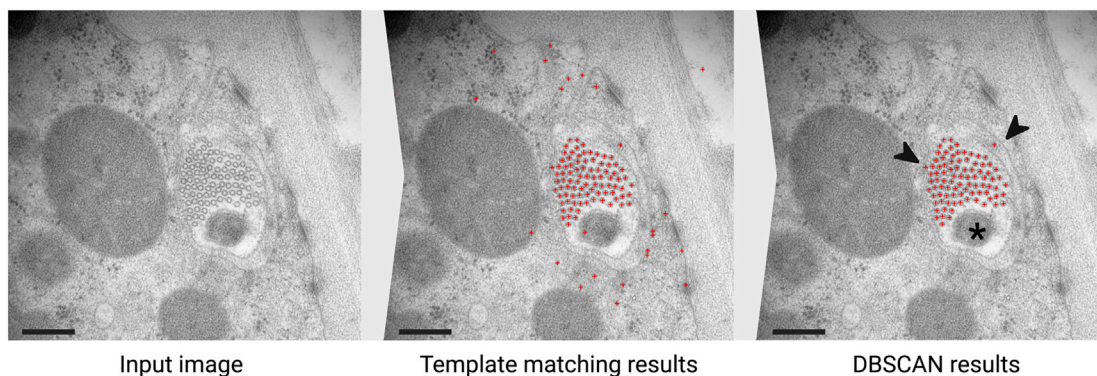


FIGURE 2 Representative images illustrating the results of the semiautomated analysis procedure. Original serial-section transmission electron micrograph (ssTEM) input image (*left*); markers indicating template match locations show false positives outside the neuron (*center*); and density-based spatial clustering of applications with noise successfully eliminates false positives that are farther away from the neuron (*right*). Manual edits are required to eliminate false positives in close proximity to the neuron (*arrowheads*). Note that the microtubule bundle shifts to accommodate the presence of mitochondria (*asterisk*). Scale bars: 0.2 μm . To see this figure in color, go online.

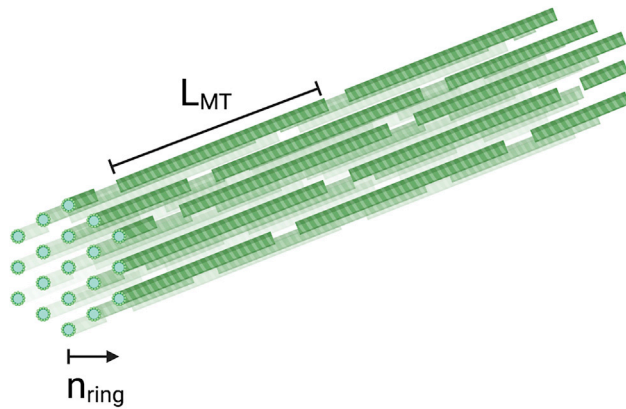


FIGURE 3 Parameters in the homogeneous axon model. The microtubules in the homogeneous models are densely packed into a hexagonal lattice. The number of rings surrounding the central microtubules is designated by n_{ring} . L_{MT} designates the length of the microtubules. The majority of the microtubules in the homogeneous model have this length, but the microtubules at either end of the model are shorter to stagger the discontinuities. To see this figure in color, go online.

Python library (44). Axon diameter measurements were obtained using ImageJ (45).

RESULTS AND DISCUSSION

Microtubule arrangement

To obtain the microtubule geometry for our image-based axon model, we analyzed a series of 300 ssTEM images collected from one *C. elegans* PLM neuron. Each image corresponds to a 50-nm section, resulting in a total segment length of 15 μm . Video S1 shows the full 3D reconstruction of the microtubules in the ssTEM data set, and Video S2 shows the aligned ssTEM image data set used to build the reconstruction. As a result of the ssTEM image analysis, we found that the number of microtubules per cross section varies along the analyzed segment of axon. The minimum and maximum values are 14 and 92, respectively, and the average number of microtubules per cross section is 61. We observed a distribution of microtubule lengths reaching as long as 12 μm but skewed toward shorter lengths with a measured average of 3.8 μm . However, this measured value underestimates the actual microtubule length because microtubules are artificially truncated at both ends of the analyzed image series. To estimate the actual average microtubule length for comparison with past measurements, we used the formula $2Na/T$ (46), where N is the average number of microtubules per cross section, a is the length of the analyzed image series, and T is the number of microtubule terminations observed in the series. Using this formula, we estimated an average microtubule length of 8.5 μm .

A previous study of the *C. elegans* posterior lateral microtubule neuron found average values of 22, 46, and 49 microtubules per cross section in three separate image series (21).

While these values differ from our measured average, they fall within the range of values we observed in our image series. The discrepancy between the averages could be due to the variation in microtubule number along the axon and the short length of the analyzed image series compared with the length of the full axon. In other organisms, a wider range of microtubule numbers has been documented, including counts in the hundreds for vertebrates and hundreds of thousands for arthropods (16,25,26).

Studies have also reported a wide range of estimates for microtubule length in neurons. Average lengths of 4.02 and 430 μm have been found in rat hippocampal (47) and frog olfactory nerve (24) neurons, respectively. In *C. elegans*, estimates range from 4.3 μm in DA9 motor neurons (22) to 20 μm in TRNs (14,48,49). Our estimate of 8.5 μm for the average microtubule length agrees with the range of 6.1–14.6 μm reported for the *C. elegans* PLM (21). This large range of reported microtubule lengths highlights the heterogeneity of axon structure not only within a single axon but among different neurons as well.

Here, we use the PLM, a *C. elegans* TRN, as a model of microtubule bundles found in many axons. Each TRN extends a long (up to 0.5 mm), slender (200–300 nm), and straight axon. These morphological characteristics enable ssTEM studies of the architecture of the microtubule bundle not only in cross section but also longitudinally (21,34,48,49). Specifically, these prior studies have used ssTEM data sets to analyze microtubule diameter, length, and intermicrotubule spacing. With an average diameter of 25 nm (48,49) and an edge-to-edge distance of 9.7 nm (34), the PLM microtubules are wider and more closely spaced than reported in other axons (16). For this current study, we sought to 1) establish an image-analysis pipeline that could support the generation of axon models with heterogeneous, image-based microtubule geometry and 2) compare heterogeneous and homogeneous geometries to improve understanding of axon damage. We prototyped this pipeline for a *C. elegans* PLM neuron as a proof of concept, but future computational studies of axon damage should consider the microtubule structures found in other neurons, which differ from the *C. elegans* PLM structure in microtubule number, length, and spacing (16).

Within the analyzed images, we identified two mitochondria present in the ssTEM data set. Fig. 2 shows an image containing the cross section of a mitochondrion marked with an asterisk. Despite the variation in the number of microtubules detected along the reconstructed axon, there was no clear correlation ($r = 0.17$, $p = 0.003$) between microtubule number and mitochondria position (stars, Fig. 4). The first mitochondrion is located in a region with microtubule numbers ranging from 24 to 31, while the second spans a region with 76–92 microtubules per cross section. The microtubule bundle does appear to shift to accommodate mitochondria, however. Future modeling studies could consider the mechanical implications of the presence of

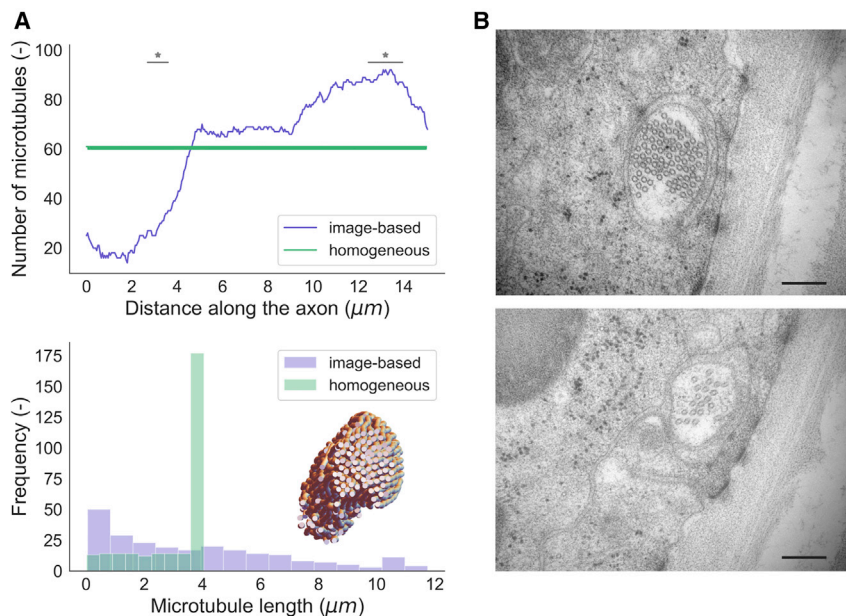


FIGURE 4 (A) Comparison of the number of microtubules per cross section and the microtubule length distribution between image-based and homogeneous axon geometries ($n_{\text{ring}} = 4, L_{MT} = 4 \mu\text{m}$). The number of microtubules per cross section varies between the extreme values of 14 and 92 in the ssTEM data set but is relatively constant in the homogeneous axon, fluctuating between 61 and 90 (top). Two mitochondria were present in the ssTEM data set (locations indicated by stars). The image-based geometry exhibits a wider distribution of microtubule lengths compared with the homogeneous geometry, in which the majority of microtubules have the same length, as illustrated by the single high bar in the lower plot (bottom). See Video S1 for the full 3D reconstruction of the microtubule geometry in the ssTEM data set (inset). (B) Example ssTEM images showing regions of high (top) and low (bottom) microtubule numbers. See Video S2 for a compilation of the full ssTEM data set used in the analysis. Scale bars: 0.2 μm . To see this figure in color, go online.

mitochondria and their linkages to both microtubules and the plasma membrane. Microtubule number does show some correlation with axon diameter ($r = 0.68$, $p < 0.001$), and the presence of mitochondria shows some association with axon diameter as well ($r = 0.40$, $p < 0.001$). While the presence of mitochondria does not provide an explanation for the variation in microtubule number along the axon, another possible explanation could be differences in mechanical loading experienced by different regions of the axon. Studies of *C. elegans* TRNs have observed that microtubule length and number differ among different neurons (14,20). Similarly, neurons are subjected to different mechanical stresses depending on their locations (14,20). It is possible that microtubule structure varies to accommodate differences in mechanical demands both between different neurons and between different regions of a single neuron.

For comparison with the heterogeneous, image-based geometry, we generated a family of homogeneous microtubule bundles to mimic existing models (28,29,31). In contrast to the ssTEM-derived geometry, the homogeneous geometries exhibit an almost constant number of microtubules per cross section with small fluctuations due to the presence of gaps between adjacent microtubules. The average number of microtubules per cross section in the homogeneous models depends on the prescribed value for the parameter n_{ring} . Most of the microtubule lengths in the homogeneous geometries are equal to the prescribed value for L_{MT} , as illustrated by the single high bar in the lower plot of Fig. 4. Some shorter microtubule lengths are present because microtubules are truncated at both ends of the model to achieve a 15- μm total axon length. Fig. 4 compares the microtubule number and length distributions for the ssTEM data and a sample homogeneous geometry with pa-

rameters set to $n_{\text{ring}} = 4$ and $L_{MT} = 4 \mu\text{m}$. The ssTEM data show more variation in microtubule length and number compared with the homogeneous geometry.

Cross-link density

To select a cross-link density value, we performed simulations of tensile loading on the image-based geometry with densities ranging from 10 to 50 cross-links per μm of microtubule length. Fig. 5 shows the resulting force-elongation curves compared with experimental data collected from *Drosophila* embryos (43). Of the five simulations, only the force-elongation curve corresponding to a density of 20 cross-links per μm remains within the range of the experimental data over the entire stretch history. For a density of 30 cross-links per μm , the force-elongation curve starts slightly outside of the experimental data at lower stretches but then curves into the range of the experimental measurements. Since the curve for a density of 30 cross-links per μm stays more toward the center of the experimental data, we selected this as the cross-link density value.

It is possible that this approach to selecting the cross-link density overestimates the density because the experimental measurements were taken on intact axons rather than solely a network of crosslinked microtubules. Other structures in the axon such as the actin-spectrin membrane periodic skeleton have been shown to contribute tensile strength (14,15,19,20). However, using the same cross-link density for both the image-based and homogeneous models facilitates the comparison of their mechanical behaviors despite uncertainty in selecting the cross-link density.

While tau has been shown to influence microtubule spacing in *C. elegans* sensory neurons, indicating a potential

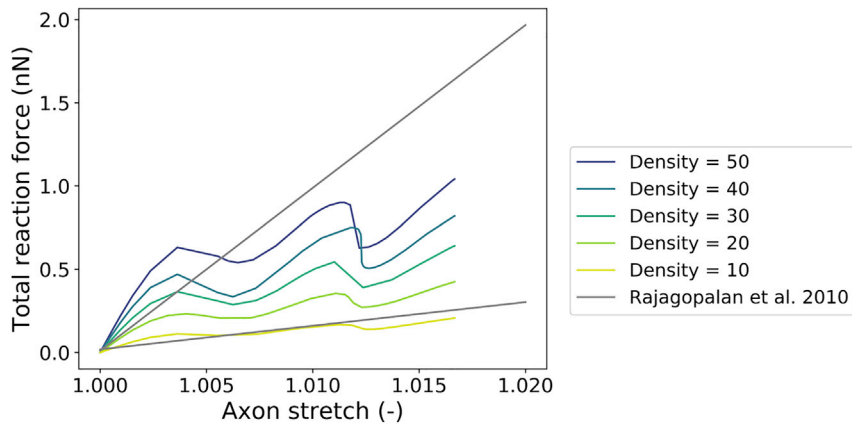


FIGURE 5 Cross-link density calibration. We calculated the force-elongation curves for tensile simulations using cross-link densities varying from 10 to 50 cross-links per μm of microtubule length. We selected a density of 30 cross-links per μm based on comparison to experimental data (43). To see this figure in color, go online.

crosslinking role (14), the role and extent of microtubule crosslinking in the neurons of other organisms is not as clear. Future studies of axon damage should consider the more loosely bundled microtubule structure found in other organisms (16).

Comparison of cross-link stretches

In comparing the deformation of the image-based and homogeneous geometries, we focused on the change in length of the cross-links within the models. For this purpose, we used the longitudinal stretch, defined as the ratio of the deformed length to the original undeformed length. In this study, we consider cross-link stretch as an indicator to identify regions of high deformation where the initiation of damage is likely to occur. However, it is also feasible that the cross-links may rupture or detach from the microtubules (28), and these failure modes should be considered in future studies of axon damage. Fig. 6 shows that in both the image-based and homogeneous models, the cross-links experience

large stretches, while the microtubules undergo little deformation. This agrees with results in other computational studies using elastic material properties (28,29). The difference between the image-based and homogeneous geometries appears in the spatial distribution of cross-link stretches. The image-based model exhibits heterogeneity in cross-link stretches with high stretches concentrated near the region with the smallest cross section. The homogeneous models exhibit a more uniform distribution of cross-link stretch along the entire length of the model.

Fig. 7 *a* plots the cross-link stretches for the image-based geometry compared with a homogeneous geometry with $n_{\text{ring}} = 4$, $L_{MT} = 4 \mu\text{m}$, corresponding to the average values of the image-based geometry. The stretches in the image-based geometry exhibit marked heterogeneity with stretches exceeding 3 in the first $5 \mu\text{m}$ but remaining below 1.5 along the remaining length. The homogeneous geometry, however, shows a more uniform distribution with stretches above 2 found along the majority of the model. The stretches decrease toward both ends of the model, likely

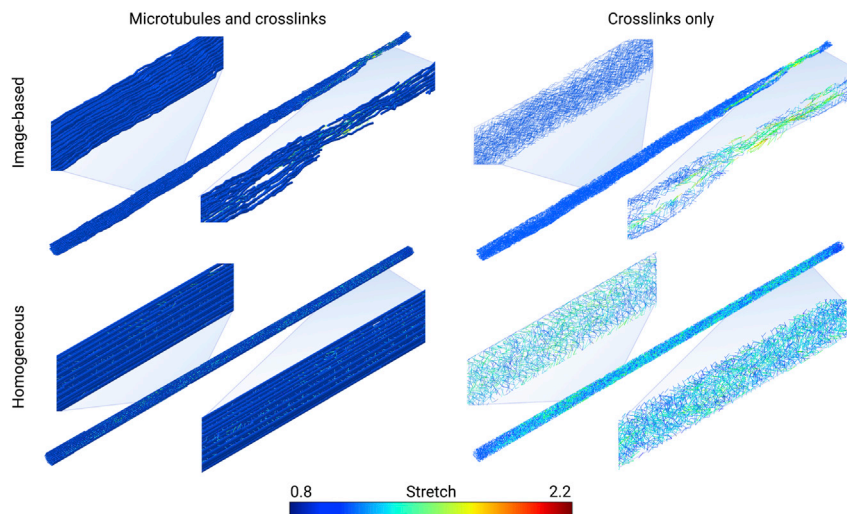


FIGURE 6 Simulation results show differences in stretch distribution between image-based and homogeneous ($n_{\text{ring}} = 4$, $L_{MT} = 4 \mu\text{m}$) models. The results are shown both with and without the microtubules to showcase the cross-links more clearly. The image-based geometry exhibits a localized region of high cross-link stretches, while the homogeneous model exhibits a more uniform distribution. To see this figure in color, go online.

due to the influence of the boundary conditions, which hold the microtubules at a prescribed displacement. In the homogeneous model, the deformation is distributed more evenly among the cross-links, and the peak stretch is lower than that of the image-based model.

The distribution of cross-link stretch in the image-based model agrees with experimental observations of heterogeneous strain in an axon subjected to tensile loading (33). Though other factors such as spatial differences in cytoskeletal contractility (50) could also contribute to the heterogeneity in axon strain, and while it is unlikely the deformation of the microtubule bundle exactly mirrors that of the entire axon, the simulations presented here suggest that heterogeneity in microtubule structure could also explain some of the heterogeneity observed in axon strain.

Fig. 7 *b* illustrates that not only the average homogeneous model with $n_{\text{ring}} = 4$, $L_{\text{MT}} = 4 \mu\text{m}$ but also models with other values for n_{ring} and L_{MT} exhibit similar cross-link stretch distributions. Changing the number of rings n_{ring} does not alter the shape of the stretch distribution, but the density of points in the stretch plots increases due to the increase in the number of cross-links in the model. As L_{MT} increases, the stretch distribution assumes more of a triangular shape with higher peak stretches exceeding that of the image-based model. It is possible that this is due to the influence of the boundary conditions at both ends of the model. At a microtubule length of $8 \mu\text{m}$, the microtubule length is longer than half of the full model length. The majority of the microtubules in the model are therefore held by the boundary conditions at either end. This leaves fewer re-

gions in the model where microtubules can slide relative to each other, resulting in higher stretches in the regions where motion is possible.

Comparison of force-elongation curves

Looking at the force-elongation curves for the image-based and homogeneous models (Fig. 8), changing the values of n_{ring} and L_{MT} changes the stiffness of the homogeneous geometry, but no single homogeneous model fully matches the mechanical behavior of the image-based geometry. While the image-based model closely matches the behavior of some homogeneous models at some portions of the stretch history, the curves never match over the entire range of stretches. For example, for the lowest values of stretch, the image-based model closely matches the homogeneous model with $L_{\text{MT}} = 4 \mu\text{m}$ and $n_{\text{ring}} = 4$. This combination of parameters corresponds to the average microtubule length and average number of microtubules per cross section in the image-based model ($3.8 \mu\text{m}$ and 61). As the stretch increases, the curve corresponding to the image-based model bends away from the curve of the homogeneous model. At intermediate stretch values, the behavior of the image-based model matches a different homogeneous model with $L_{\text{MT}} = 4 \mu\text{m}$ and $n_{\text{ring}} = 2$. This corresponds to a homogeneous model with 19 microtubules per cross section, which is comparable to 14, the minimum value in the image-based geometry.

The wavy shape of the force-elongation curve corresponding to the image-based model could result from the inward collapse of microtubules since lateral motion is not

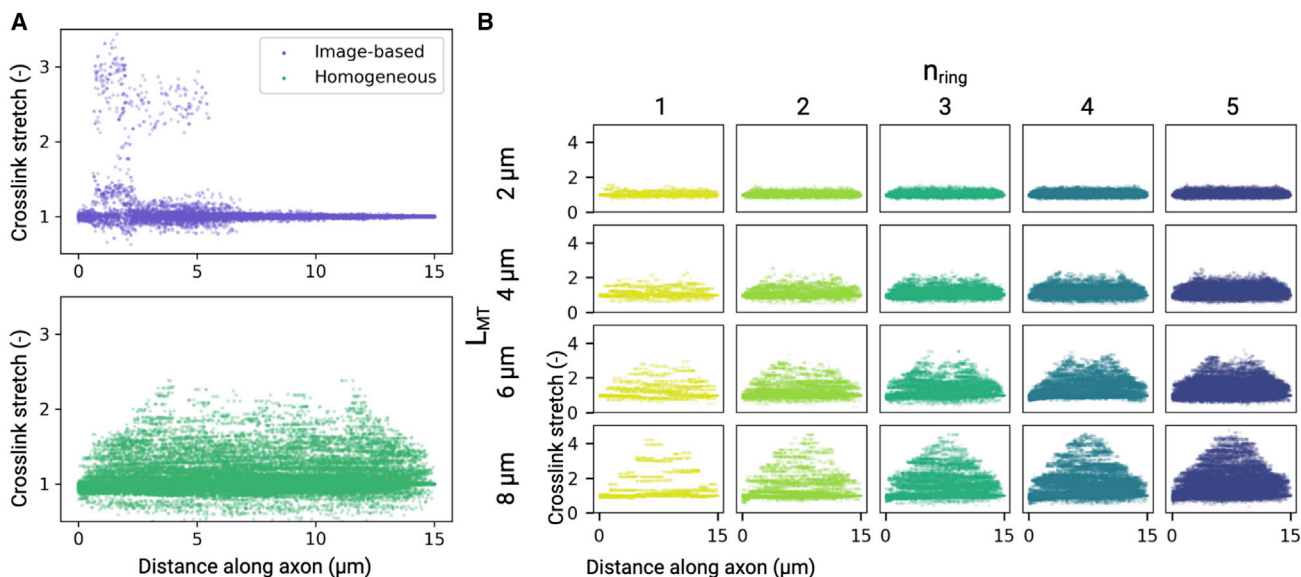


FIGURE 7 (A) Comparison of cross-link stretch distribution between image-based and homogeneous models ($n_{\text{ring}} = 4$, $L_{\text{MT}} = 4 \mu\text{m}$). The image-based model has both a region of high peak cross-link stretch and a region that experiences little deformation. In the homogeneous model, the cross-link stretch distribution remains relatively constant throughout the model. (B) Cross-link stretch distributions of homogeneous models with various L_{MT} and n_{ring} values. Changing n_{ring} does not affect the shape of the cross-link stretch distribution but increasing L_{MT} leads to a more triangular shape with higher peak cross-link stretches. To see this figure in color, go online.

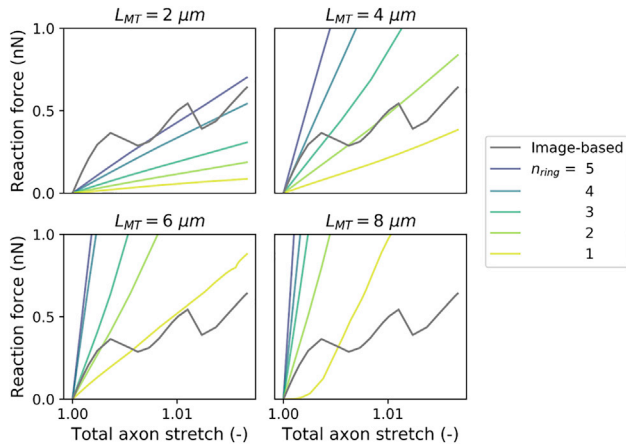


FIGURE 8 Force-elongation curves for image-based and homogeneous geometries. While the stiffness of the homogeneous model can be tuned by changing n_{ring} and L_{MT} , no single combination of parameters creates a homogeneous model that replicates the behavior of the image-based model across all stretch magnitudes. To see this figure in color, go online.

constrained in the simulation. It is likely that this does not occur in the axon cytoskeleton due to the presence of other cytoskeletal components such as neurofilaments, which may limit the lateral translation of microtubules (18).

Spring analogy

To understand the difference between the image-based and homogeneous geometries, we consider an analogy of springs in series in Fig. 9. The image-based, heterogeneous geometry is represented by n springs of stiffness k in series with one spring of stiffness $a \times k$, and $a < 1$ so that one of the springs is less stiff than all others. This corresponds to the weakest cross section in the axon cytoskeleton. In contrast, we represent the homogeneous geometry by $n+1$ springs all of stiffness $b \times k$. The parameter b determines the stiffness of the homogeneous geometry relative to that of the heterogeneous geometry. Setting $b = 1$ makes the stiffness of the homogeneous model equal to the stiffest portion of the heterogeneous model. Alternatively, setting $b = a$ makes the stiffness of the homogeneous model equal to the most compliant portion of the heterogeneous model.

The effective stiffnesses of the heterogeneous model, k_{eff}^{het} , and homogeneous model, k_{eff}^{hom} , are

$$k_{eff}^{het} = \frac{ak}{an+1} \text{ and } k_{eff}^{hom} = \frac{bk}{n+1}. \quad (1)$$

Using these expressions, we derive the following equation for the change in length, Δx_i^{het} , of the most compliant spring in the heterogeneous model,

$$F^{het} = k_{eff}^{het} \Delta x_{tot} = ak \Delta x_i^{het}, \quad (2)$$

where F^{het} is the force pulling on the axon, Δx_{tot} is the total change in length, and Δx_i^{het} is the change in the length of the

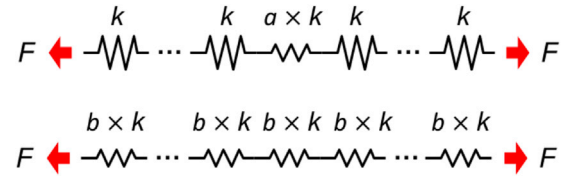


FIGURE 9 A simple spring analogy compares a heterogeneous model of springs in series to a homogeneous model. Analysis of these simple systems provides an explanation for higher local stretches in a heterogeneous system compared with a homogeneous system when subjected to the same global stretch. To see this figure in color, go online.

compliant spring. All of the springs in the homogeneous model undergo the same change in length,

$$F^{hom} = k_{eff}^{hom} \Delta x_{tot} = bk \Delta x_i^{hom}, \quad (3)$$

where F^{hom} is the pulling force, Δx_{tot} is the total change in length as before, and Δx_i^{hom} is the change in length of a single spring in the homogeneous model. For the same global change in length, Δx_{tot} , the ratio of the change in length of the heterogeneous model spring to that of the homogeneous model is

$$\frac{\Delta x_i^{het}}{\Delta x_i^{hom}} = \frac{b}{a} \frac{k_{eff}^{het}}{k_{eff}^{hom}} = \frac{n+1}{an+1}. \quad (4)$$

The final expression for the ratio does not depend on b , and since $a < 1$, Δx_i^{het} is greater than Δx_i^{hom} for any value of b . The change in length of the springs is analogous to local stretches in the axon simulations. Therefore, this spring model analogy confirms that the peak local stretch in a heterogeneous axon model will always be higher than the peak local stretch in a homogeneous model when subjected to the same global stretch.

Model limitations

While our model focuses on microtubules and crosslinking proteins, other components of the axon cytoskeleton also contribute to the mechanical behavior of the axon. For instance, recent studies have shown that the cortical corset acts as a stiffening element in parallel with microtubules (15,51). Furthermore, our model does not consider neurofilaments found in many, but not all, axons (16). We plan to study the effects of these additional cytoskeletal components in our future studies. However, for the present study, the importance of using heterogeneous, rather than homogeneous, geometries can be seen already in considering just the microtubules in their bundled state.

In this study, we use elastic material properties for both the microtubules and cross-links in the models. With these material properties, it is possible to compare heterogeneous and homogeneous geometries in response to static or quasi-static loading. However, the study of different loading rates will require the incorporation of time-dependent properties.

This could be done by including viscoelastic material parameters (52) or by incorporating dynamic attachment and detachment of cross-links (30,32).

The current model does not account for plausible dynamic molecular mechanisms affecting the axon's response to mechanical stimulation, including the attachment and detachment of crosslinking proteins. We currently model cross-links as fixed in their position along the microtubules, but dynamic attachment and detachment could affect the resulting deformation of the microtubule bundle (14,32). In prior work, we developed computational tools to address these factors in the context of a homogeneous geometry (32). Future studies merging both approaches will enhance understanding of the mechanisms that make axons susceptible or resistant to mechanical damage.

In our model, we constrain the motion of the microtubules by fixing the rotational degrees of freedom. A previous study found that simplifying the kinematics of the microtubule bundle aids the convergence of damage simulations but decreases the strains seen in the microtubules (31). However, the strains in the constrained simulations remain proportional to the strains in the unconstrained simulations, so the unconstrained results can be approximated by applying a correction factor to the constrained results. Since we use the same constraints for both the heterogeneous and homogeneous geometries, we expect that both models will be affected similarly by the boundary conditions, allowing direct comparison of the simulation results. However, in future axon damage threshold studies with heterogeneous geometries, the effect of these constraints should be taken into account.

Finally, the *C. elegans* PLM we used in this study to demonstrate the image-based model generation procedure exhibits a tightly bundled microtubule architecture that differs from the organization of microtubules in other neurons and other organisms (14,16). Microtubules among different neurons and organisms differ in number, length, and spacing (16). Future simulations of axon damage thresholds should take into consideration the varied microtubule architectures found in other neurons.

CONCLUSIONS

The use of computational models to predict head injury depends on the selection of an accurate axon damage threshold. While homogeneous models overestimate axon strength, our image-based approach to generating microtubule geometry takes into account the heterogeneity of the axonal cytoskeleton and includes the presence of weaker cross sections that are more susceptible to damage. Simulations of tensile loading on the image-based microtubule geometry result in a heterogeneous distribution of cross-link stretches with the highest stretches occurring near the weakest cross sections, indicating spatial variation in susceptibility to damage. In contrast, the homogeneous models exhibit

a more uniform distribution of cross-link stretches. Our results demonstrate that heterogeneity plays a key role governing the initiation of failure in axon damage simulations. This emphasizes the need to consider structural heterogeneity as an important parameter in future models studying axon damage thresholds.

Beyond determining failure thresholds, the image-based model generation procedure we present here could be applied to investigate the microtubule structure in damaged axons and to compare the microtubule structures of different neuron populations. Simulations of mechanical loading on the resulting models could shed light on differences in susceptibility to injury. Furthermore, the image analysis pipeline could be easily adapted to analyze different structures in serial-section data sets by using different template images in the template matching step. This has the potential to speed up analysis in any study involving serial-section image sets.

SUPPORTING MATERIAL

Supporting material can be found online at <https://doi.org/10.1016/j.bpj.2022.11.2946>.

AUTHOR CONTRIBUTIONS

L.M.W., M.B.G., and E.K. designed the study. L.M.W. performed the simulations and analyzed the data. L.M.W., M.B.G., and E.K. wrote the manuscript.

ACKNOWLEDGMENTS

Fig. 3 was generated using biorender.com. This work was supported by the National Science Foundation Graduate Research Fellowship DGE 1656518, the Bio-X Bowes Fellowship, and the Stanford School of Engineering Fellowship to L.M.W. and by grants to M.B.G. (National Institute of Neurological Disorders and Stroke, R35NS105092) and E.K. (National Science Foundation grant CMMI 1727268).

DECLARATION OF INTERESTS

The authors declare no competing interests.

REFERENCES

1. Dewan, M. C., A. Rattani, ..., K. B. Park. 2018. Estimating the global incidence of traumatic brain injury. *J. Neurosurg.* 130:1080–1097.
2. Corrigan, J. D., A. W. Selassie, and J. A. L. Orman. 2010. The epidemiology of traumatic brain injury. *J. Head Trauma Rehabil.* 25:72–80.
3. Arciniegas, D. B., K. Held, and P. Wagner. 2002. Cognitive impairment following traumatic brain injury. *Curr. Treat. Options Neurol.* 4:43–57.
4. Hill, C. S., M. P. Coleman, and D. K. Menon. 2016. Traumatic axonal injury: mechanisms and translational opportunities. *Trends Neurosci.* 39:311–324.
5. Smith, D. H., M. Nonaka, ..., D. F. Meaney. 2000. Immediate coma following inertial brain injury dependent on axonal damage in the brainstem. *J. Neurosurg.* 93:315–322.

6. Johnson, V. E., W. Stewart, and D. H. Smith. 2013. Axonal pathology in traumatic brain injury. *Exp. Neurol.* 246:35–43.
7. Miller, L. E., J. E. Urban, ..., J. D. Stitzel. 2021. Brain strain: computational model-based metrics for head impact exposure and injury correlation. *Ann. Biomed. Eng.* 49:1083–1096.
8. Li, X., Z. Zhou, and S. Kleiven. 2021. An anatomically detailed and personalizable head injury model: significance of brain and white matter tract morphological variability on strain. *Biomech. Model. Mechanobiol.* 20:403–431.
9. Sahoo, D., C. Deck, and R. Willinger. 2016. Brain injury tolerance limit based on computation of axonal strain. *Accid. Anal. Prev.* 92:53–70.
10. Mohammadipour, A., and A. Alemi. 2017. Micromechanical analysis of brain's diffuse axonal injury. *J. Biomech.* 65:61–74.
11. Kurtoglu, E., H. Nakadate, ..., A. Kakuta. 2017. Uniaxial stretch-induced axonal injury thresholds for axonal dysfunction and disruption and strain rate effects on thresholds for mouse neuronal stem cells. *J. Biomech. Sci. Eng.* 12:16–00598.
12. Tang-Schomer, M. D., V. E. Johnson, ..., D. H. Smith. 2012. Partial interruption of axonal transport due to microtubule breakage accounts for the formation of periodic varicosities after traumatic axonal injury. *Exp. Neurol.* 233:364–372.
13. Geddes, D. M., R. S. Cargill, 2nd, and M. C. Laplace. 2003. Mechanical stretch to neurons results in a strain rate and magnitude-dependent increase in plasma membrane permeability. *J. Neurotrauma.* 20:1039–1049.
14. Krieg, M., J. Stühmer, ..., M. B. Goodman. 2017. Genetic defects in β -spectrin and tau sensitize C. Elegans axons to movement-induced damage via torque-tension coupling. *Elife.* 6:e20172.
15. Dubey, S., N. Bhembre, ..., P. Pullarkat. 2020. The axonal actin-spectrin lattice acts as a tension buffering shock absorber. *Elife.* 9:e51772.
16. Prokop, A. 2020. Cytoskeletal organization of axons in vertebrates and invertebrates. *J. Cell Biol.* 219:e201912081.
17. Conde, C., and A. Cáceres. 2009. Microtubule assembly, organization and dynamics in axons and dendrites. *Nat. Rev. Neurosci.* 10:319–332.
18. Wong, P. C., J. Marszalek, ..., D. W. Cleveland. 1995. Increasing neurofilament subunit NF-M expression reduces axonal NF-H, inhibits radial growth, and results in neurofilamentous accumulation in motor neurons. *J. Cell Biol.* 130:1413–1422.
19. Xu, K., G. Zhong, and X. Zhuang. 2013. Actin, spectrin, and associated proteins form a periodic cytoskeletal structure in axons. *Science.* 339:452–456.
20. Krieg, M., A. R. Dunn, and M. B. Goodman. 2014. Mechanical control of the sense of touch by β -spectrin. *Nat. Cell Biol.* 16:224–233.
21. Chalfie, M., and J. N. Thomson. 1979. Organization of neuronal microtubules in the nematode *Caenorhabditis elegans*. *J. Cell Biol.* 82:278–289.
22. Yogeve, S., R. Cooper, ..., K. Shen. 2016. Microtubule organization determines axonal transport dynamics. *Neuron.* 92:449–460.
23. Bray, D., and M. B. Bunge. 1981. Serial analysis of microtubules in cultured rat sensory axons. *J. Neurocytol.* 10:589–605.
24. Burton, P. R. 1987. Microtubules of frog olfactory axons: their length and number/axon. *Brain Res.* 409:71–78.
25. Hoffman, P. N., J. W. Griffin, and D. L. Price. 1984. Control of axonal caliber by neurofilament transport. *J. Cell Biol.* 99:705–714.
26. Nadelhaft, I. 1974. Microtubule densities and total numbers in selected axons of the crayfish abdominal nerve cord. *J. Neurocytol.* 3:73–86.
27. Ouyang, H., E. Nauman, and R. Shi. 2013. Contribution of cytoskeletal elements to the axonal mechanical properties. *J. Biol. Eng.* 7:21.
28. de Rooij, R., and E. Kuhl. 2018. Microtubule polymerization and cross-link dynamics explain axonal stiffness and damage. *Biophys. J.* 114:201–212.
29. Peter, S. J., and M. R. K. Mofrad. 2012. Computational modeling of axonal microtubule bundles under tension. *Biophys. J.* 102:749–757.
30. Ahmadzadeh, H., D. H. Smith, and V. B. Shenoy. 2015. Mechanical effects of dynamic binding between tau proteins on microtubules during axonal injury. *Biophys. J.* 109:2328–2337.
31. Montanino, A., and S. Kleiven. 2018. Utilizing a structural mechanics approach to assess the primary effects of injury loads onto the axon and its components. *Front. Neurol.* 9:643.
32. de Rooij, R., and E. Kuhl. 2018. Physical biology of axonal damage. *Front. Cell. Neurosci.* 12:144.
33. Chetta, J., C. Kye, and S. B. Shah. 2010. Cytoskeletal dynamics in response to tensile loading of mammalian axons. *Cytoskeleton.* 67:650–665.
34. Cueva, J. G., and M. B. Goodman. 2007. Serial section electron microscopy data of touch receptor neurons from wild type animals using a mouse polyclonal antibody against MEC-2. *Stanford Digital Repository.* <http://purl.stanford.edu/gq316wm6430>.
35. Cueva, J. G., A. Mulholland, and M. B. Goodman. 2007. Nanoscale organization of the MEC-4 DEG/ENaC sensory mechanotransduction channel in *Caenorhabditis elegans* touch receptor neurons. *J. Neurosci.* 27:14089–14098.
36. Gittes, F., B. Mickey, ..., J. Howard. 1993. Flexural rigidity of microtubules and actin filaments measured from thermal fluctuations in shape. *J. Cell Biol.* 120:923–934.
37. Suresh, S. 2007. Biomechanics and biophysics of cancer cells. *Acta Biomater.* 3:413–438.
38. Mallik, R., B. C. Carter, ..., S. P. Gross. 2004. Cytoplasmic dynein functions as a gear in response to load. *Nature.* 427:649–652.
39. de Rooij, R., K. E. Miller, and E. Kuhl. 2017. Modeling molecular mechanisms in the axon. *Comput. Mech.* 59:523–537.
40. Bradski, G. 2000. The OpenCV library. *Dr. Dobbs's J. Softw. Tools.* 120:122–125.
41. Pedregosa, F., G. Varoquaux, ..., E. Duchesnay. 2011. Scikit-learn: machine learning in Python. *J. Mach. Learn. Res.* 12:2825–2830.
42. Khallaghi, S. 2021. Python-CPD. <https://github.com/siavashk/pycpd>.
43. Rajagopalan, J., A. Tofangchi, and M. T. A. Saif. 2010. Drosophila neurons actively regulate axonal tension in vivo. *Biophys. J.* 99:3208–3215.
44. Virtanen, P., R. Gommers, ..., SciPy 10 Contributors. 2020. SciPy 1.0: fundamental algorithms for scientific computing in Python. *Nat. Methods.* 17:261–272.
45. Schneider, C. A., W. S. Rasband, and K. W. Eliceiri. 2012. NIH Image to ImageJ: 25 years of image analysis. *Nat. Methods.* 9:671–675.
46. Hardham, A. R., and B. E. Gunning. 1978. Structure of cortical microtubule arrays in plant cells. *J. Cell Biol.* 77:14–34.
47. Yu, W., and P. W. Baas. 1994. Changes in microtubule number and length during axon differentiation. *J. Neurosci.* 14:2818–2829.
48. Chalfie, M., and J. N. Thomson. 1982. Structural and functional diversity in the neuronal microtubules of *Caenorhabditis elegans*. *J. Cell Biol.* 93:15–23.
49. Cueva, J. G., J. Hsin, ..., M. B. Goodman. 2012. Posttranslational acetylation of α -tubulin constrains protofilament number in native microtubules. *Curr. Biol.* 22:1066–1074.
50. Mutalik, S. P., J. Joseph, ..., A. Ghose. 2018. Cytoskeletal mechanisms of axonal contractility. *Biophys. J.* 115:713–724.
51. Costa, A. R., S. C. Sousa, ..., M. M. Sousa. 2020. The membrane periodic skeleton is an actomyosin network that regulates axonal diameter and conduction. *Elife.* 9:e55471.
52. Ahmadzadeh, H., D. H. Smith, and V. B. Shenoy. 2014. Viscoelasticity of tau proteins leads to strain rate-dependent breaking of microtubules during axonal stretch injury: predictions from a mathematical model. *Biophys. J.* 106:1123–1133.